PAPER

Probing the interaction of Rh, Co and bimetallic Rh–Co nanoparticles with the CeO$_2$ support: catalytic materials for alternative energy generation†

E. Varga,[a] P. Pusztai,[b] L. Óvári,[c] A. Oszkó,[a] A. Erdőhelyi,[a] C. Papp,[d] H.-P. Steinrück,[d] Z. Kónya[bc] and J. Kiss*[ac]

The interaction of CeO$_2$-supported Rh, Co and bimetallic Rh–Co nanoparticles, which are active catalysts in hydrogen production *via* steam reforming of ethanol, a process related to renewable energy generation, was studied by X-ray diffraction (XRD), high resolution electron microscopy (HRTEM), X-ray photoelectron spectroscopy (XPS) and low energy ion scattering (LEIS). Furthermore, diffuse reflectance infrared spectroscopy (DRIFTS) of adsorbed CO as a probe molecule was used to characterize the morphology of metal particles. At small loadings (0.1%), Rh is in a much dispersed state on ceria, while at higher contents (1–5%), Rh forms 2–8 nm particles. Between 473–673 K pronounced oxygen transfer from ceria to Rh is observed and at 773 K significant agglomeration of Rh occurs. On reduced ceria, XPS indicates a possible electron transfer from Rh to ceria. The formation of smaller ceria crystallites upon loading with Co was concluded from XRD and HRTEM; for 10% Co, the CeO$_2$ particle size decreased from 27.6 to 10.7 nm. A strong dissolution of Co into ceria and a certain extent of encapsulation by ceria were deduced by XRD, XPS and LEIS. In the bimetallic system, the presence of Rh enhances the reduction of cobalt and ceria. During thermal treatments, reoxidation of Co occurs, and Rh agglomeration as well as oxygen migration from ceria to Rh are hindered in the presence of cobalt.

1. Introduction

Hydrogen is expected to play a key role in future energy technology as an efficient energy carrier.[1–3] Great efforts are currently made to produce hydrogen by heterogeneous catalytic processes from renewable sources. This demand inspired studies on the dehydrogenation of oxygenated hydrocarbons including alcohols. These materials, which are obtained by the fermentation of agricultural wastes, can be important carbon-neutral renewable energy sources, and also renewable raw materials for the chemical industry.[4–7]

Ceria-supported precious metal catalysts such as Rh, Pd, and Pt are widely used in many important applications, including three-way automobile emission-control catalysis, fuel cells, and also hydrogen production from ethanol. This is due to the peculiar redox properties and oxygen storage capacity of ceria, as well as to synergetic effects between the ceria support and metals.[8–13] Noble metals, especially Rh, have proven to be excellent catalysts for dehydrogenation reactions,[14–16] but their prices are prohibitively high. As an alternative, the less expensive transition metal Co is a promising catalyst for the steam reforming of ethanol (SRE). As a consequence of the Co-promoted C–C bond rupture in adsorbed ethanol, Co on CeO$_2$ and on other supports achieves high ethanol conversion and selectivities of H$_2$ and CO$_2$, even at relatively low temperatures ($\sim$723 K).[17–19] While recent studies suggested that Co^{2+} sites are the active centers in SRE, and that Co^0 sites are responsible for coke formation,[20,21] other authors argue that metallic cobalt plays the key role in SRE.[21] The oxygen exchange capacity of cerium oxide is associated with its ability to reversibly change the oxidation states between Ce^{4+} and Ce^{3+}. These observations led to the outstanding attention on the catalytic properties of the Co/ceria system in ethanol transformation reactions, including SRE.[12,17–28]

Very recently we have found that trace amounts of Rh promoter (0.1 wt%–0.17 mol%) dramatically altered the reaction pathways of SRE on Co/ceria catalysts. In contrast to Co/ceria, on rhodium-containing Co/ceria catalysts no acetone was observed.

^{a} *Department of Physical Chemistry and Materials Science, University of Szeged, Aradi v.t. 1, H-6720 Szeged, Hungary. E-mail: jkiss@chem.u-szeged.hu*

^{b} *Department of Applied and Environmental Chemistry, University of Szeged, H-6720 Szeged, Hungary*

^{c} *MTA-SZTE Reaction Kinetics and Surface Chemistry Research Group, Rerrich B. t. 1, H-6720 Szeged, Hungary*

^{d} *Chair of Physical Chemistry II, University of Erlangen-Nürnberg, Egerlandstr. 3, 91058 Erlangen, Germany*

† Electronic supplementary information (ESI) available. See DOI: 10.1039/c5cp03549j

27154 | *Phys. Chem. Chem. Phys.*, 2015, **17**, 27154–27166

This journal is © the Owner Societies 2015

The addition of a small amount of Rh as a promoter, however, resulted in a significant increase in the hydrogen selectivity.[29,30] Bimetallic Rh–Co catalysts supported on MgO showed also high activity in the partial oxidation of methane.[31,32] Similar catalytic systems (Pt–Ni, Pd–Ni, Rh–Ni) give high methane conversion in the oxidative steam reforming of CH_4.[33–35] Rh containing bimetallic catalysts show high efficiencies in dry[36] and steam[35] reforming of methane.

Recently, it was demonstrated that the catalytic performance of CeO_2 depends on the particle size, due to the difference of the reducibility and therefore the number of acidic sites.[37] Depending on the degree of ceria reduction, unique reactivity profiles can also be observed on ceria-supported Rh catalysts. For example, while CO adsorbs non-dissociatively on Rh nanoparticles on fully oxidized ceria films, it dissociates on partially reduced films.[34] Similarly, NO dissociation is enhanced when Rh particles are supported on reduced CeO_2(111).[38] Several hypotheses have been put forward, including electron transfer from ceria to Rh particles, structural variation in the Rh particles, or O spillover from Rh to ceria.[35,36] Low-temperature oxygen migration from ceria to Rh is also proposed in the ceria–rhodium interaction.[37,38]

The growth of Co on CeO_2(111) was briefly studied previously using XPS. Based on the linear dependence of the Ce 3d/Co 2p intensity ratio vs. cobalt coverage, two dimensional growth of Co was proposed up to 1 ML.[21] Recent low energy ion scattering spectroscopy (LEIS) and XPS studies showed, however, that the growth mode is rather three dimensional.[39] From the Co 2p peak shape, the resulting surface species were identified as Co^0 and Co^{2+}. Furthermore, reduction of Ce was observed upon Co deposition, due to the reaction of Co with CeO_2.[21,28,39] A significant part of cobalt (Co^{2+}) dissolved into the CeO_2(111) film, as was detected by LEIS.[39] On mesoporous ceria, metallic cobalt cannot be prepared using cobalt salts as a precursor. Even after strong reduction with hydrogen, the majority of cobalt remained in the oxidized Co^{2+} state.[24,25,29,30] When a small amount (0.1%) of Rh was added to the Co/ceria system, the reducibility was enhanced dramatically. This was concluded from the reaction temperature of cobalt during temperature reduction experiments (TPR) and from the lower binding energy of the Co 2p signal in XPS. In addition, the ceria support was also reduced significantly. These effects can be explained by a hydrogen spill over phenomenon.[29,30] Similar noble metal-induced effects were observed for alumina-supported cobalt Fischer–Tropsch catalysts,[40,41] and on other bimetallic cobalt-based systems.[36,42–44]

It is frequently observed that the presence of a second metal can greatly influence the intrinsic surface properties of a specific metal. It is emphasized that in contrast to bulk alloys, nanosized bimetallic systems are extremely sensitive to the structure, morphology, and valence state of the oxide support, on which the nanoparticles were prepared.[45,46] "Ensemble" or "ligand" effects are frequently invoked to explain the promoting effect of the second metal.[44] Enhanced dispersion[47] and increased sintering of Au nanoparticles on TiO_2(110) were observed in the presence of a second metal.[48] It was also observed

that the second metal (Rh, Pt, and Pd) significantly changed the morphology, topology and reactivity of the other metal (Au and Mo) on oxides.[49–53] STM and LEIS experiments revealed that the metal may completely and uniformly cover the second metal nanoparticles.[54,55]

An important aim of this study is to understand the enhanced catalytic effects of the ceria-supported Rh–Co bimetallic catalyst in SRE. For this purpose, we map a variety of possible interactions between rhodium and cobalt on the ceria support. As ceria itself is an active support in mono- and bimetallic catalysts, the metal-support interaction is also examined. X-ray diffraction (XRD) and high resolution transmission electron microscopy (HRTEM) give valuable data about the structure and morphology of nanoparticles. X-ray photoelectron spectroscopy (XPS) is an excellent tool to describe the oxidation states of the elements and to follow the charge transfer from metal to metal, and from the metal to the support and back in mono and bimetallic catalysts.[56,57] While XPS provides important data from the top surface layers of a sample (down to a depth of a few nanometers), LEIS supplies information almost exclusively about the outermost atomic layer.[58,59] These two methods, complemented with energy-dispersive X-ray spectroscopy (EDX), provide a comprehensive characterization of the surface and bulk composition of complex catalytic systems.

Herein, we first investigate Rh/ceria catalysts, then we focus on the Co/ceria systems and finally turn to ceria supported Rh–Co bimetallic catalysts. As a dramatic influence on the catalytic properties in the steam reforming of ethanol was observed even for very small amounts of Rh promoter, investigations concentrate mainly on (0.1 wt% Rh + 2 wt% Co)/CeO_2 and on (0.1 wt% Rh + 10 wt% Co)/CeO_2 catalysts. Moreover, in order to get closer to the catalytic conditions, we applied the same pretreatment that was used in the catalytic reactions.

2. Experimental

The catalysts were prepared by impregnating the CeO_2 support (Alfa Aesar, 43 m^2 g^{-1}) with the aqueous solution of $Co(NO_3)_2$ to yield nominal metal contents of 2 wt% (5.6 mol%) or 10 wt% (28.0 mol%). The impregnated powders were dried at 383 K, calcined at 973 K and pressed to pellets. Rh containing samples (0.1 wt% = 0.17 mol%, 1 wt% = 1.7 mol%, 5 wt% = 8.5 mol%) were prepared by the same impregnation method from $RhCl_3 \cdot$ $3H_2O$ (Johnson Matthey). Prior to impregnation, the ceria support was calcined at 973 K. The Rh–Co bimetallic samples were prepared by sequential impregnation and calcination with Co, and thereafter with Rh.[29] Before the measurements, fragments of catalyst pellets were oxidized at 673 K in flowing O_2 for 20 min and reduced at 773 K in flowing H_2 for 60 min. The hydrogen was replaced by nitrogen within few seconds, and the sample was cooled down in an inert atmosphere. In our XPS measurements it was observed that on the ceria-supported samples only minor amounts of adventitious carbon adsorb, and that at high Rh content a distinct Cl 2p peak is also present on the survey spectra, which originated from the $RhCl_3$ reagent.

Table 1 Some physical parameters of bare supports and Co and Rh loaded catalysts[a]

Catalyst[a]	S_A (m^2 g^{-1})	Total pore volume (cm^3 g^{-1}) at p/p_0 = 0.99	Average pore radius (nm)	CeO$_2$ particle size[b] (nm)	Co/Rh atomic ratio
CeO$_2$	21.5	0.156	14.5	27.6	—
2% Co/CeO$_2$	7.4	0.045	12.3	17.1	—
10% Co/CeO$_2$	6.8	0.041	11.7	10.7	—
0.1% Rh/CeO$_2$	19.8	0.148	14.2	27.6	—
0.1% Rh + 2% Co/CeO$_2$	7.6	0.050	13.3	17.0	34.9
1% Rh/CeO$_2$	18.6	0.120	13	26.7	—
5% Rh/CeO$_2$	17.0	0.109	12.5	26.5	—
0.1% Rh + 10% Co/CeO$_2$	6.9	0.048	13.1	11.1	174.5
1% Rh + 2% Co/CeO$_2$	7.8	0.050	12.8	24.1	3.5

[a] The samples were calcined at 973 K. [b] Determined from XRD after reduction.

After pretreatment all these contaminants were found to be removed (Fig. S1, ESI†).

The BET surface and pore volume measurements of the catalysts were carried out using a Quantachrome NOVA 3000e instrument using N$_2$ adsorption at liquid nitrogen temperature (Table 1). The surface areas and pore sizes are consistent with a mesoporous material.[25,29]

For XPS studies, the powder samples were pressed into pellets with *ca.* 1 cm diameter and a few tenth of mm thickness. Sample treatments were carried out in a high-pressure cell (catalytic chamber) connected to the analysis chamber *via* a gate valve. The samples were pre-treated in the same way as described above. After the pre-treatment, they were cooled down to room temperature in flowing nitrogen. Then, the high-pressure cell was evacuated; the sample was transferred to the analysis chamber in high vacuum (*i.e.*, without contact to air), where the XP spectra were recorded. As the next step, the sample was moved back into the catalytic chamber, where it was heated under flowing N$_2$ up to 773 K in 100 K steps. XP spectra were recorded using a SPECS instrument equipped with a PHOIBOS 150 MCD 9 hemispherical electron energy analyzer, using Al K$_\alpha$ radiation ($h\nu$ = 1486.6 eV). The X-ray gun was operated at 210 W (14 kV, 15 mA). The analyzer was operated in the FAT mode, with the pass energy set to 20 eV. The detection angle of electrons was 20° with respect to surface normal. Typically five scans were summed to get a single spectrum. For data acquisition and evaluation both manufacturer's (SpecsLab2) and commercial (CasaXPS, Origin) software were used. The binding energy scale was corrected by fixing the Ce 3d u$'''$ peak (see below) to 916.6 eV. The deconvolution of the high-resolution spectra was performed using the curved background type and the symmetric components were fitted with a common Gaussian–Lorentzian (70 : 30) line shape. For Rh 3d and Co 2p signals, the peak shapes of metallic Rh and Co, CoO and Co$_3$O$_4$ reference samples were applied.

A SPECS IQE 12/38 ion source was used for LEIS spectra. He$^+$ or Ne$^+$ ions of 800 eV kinetic energy were applied at a low ion flux (0.2 µA cm^{-2}), which was necessary to minimize the sputtering of the surface. During acquisition the samples were flooded with electrons possessing 1–2 eV energy to compensate the electrostatic charging. The incident angle was 55° (with respect to surface normal), ions ejected along the surface normal were detected. The ion energies were measured using the same hemispherical energy analyzer as mentioned above. Etching processes were performed using the same ion source with the use of 4 keV Ar$^+$ ions up to 0.7 µA cm^{-2} ion flux.

DRIFT spectra were recorded using an Agilent CARY-670 FTS-135 FT-IR spectrometer equipped with a diffuse reflectance attachment (Harrick) with BaF$_2$ windows. Typically 256 scans were registered at a spectral resolution of 2 cm^{-1}. All spectra were recorded at 293 K. The whole optical path was purged with CO$_2$- and H$_2$O-free air generated by a Whatman purge gas generator.

The bulk concentration of the elements was determined by energy-dispersive X-ray spectroscopy (EDX) using an Röntec-Quantax QX^2 spectrometer built into a Hitachi S-4700 type II cold field emission scanning electron microscope. Spectra were taken at a 20 kV acceleration voltage and quantitatively analyzed by the factory standard software after automatic background subtraction and peak fitting.

The morphology of ceria and metal-modified ceria was characterized by transmission electron microscopy (FEI Tecnai G^2 20 X-Twin; 200 kV operation voltage, ×180 000 magnification, 125 pm per pixel resolution). X-ray diffractometry (RigakuMini-FlexII; CuK$_\alpha$) and electron diffraction were used to determine the crystallinity and the structure. The metal particle size distribution was determined by image analysis of the HRTEM pictures using ImageJ software. At least five representative images of equal magnification, taken at different spots of the TEM grid were first subjected to rolling ball background subtraction and contrast enhancement, and then the diameter of the metal nanoparticles in the image was manually measured against the calibrated TEM scale bar. Each diameter distribution histogram was constructed from 200 individual nanoparticle diameter measurements.

3. Results and discussion

3.1 Reducibility of ceria, Rh/ceria, Co/ceria, bimetallic/ceria catalysts and catalytic test in the SRE

The reducibility of ceria and metal-modified ceria is very sensitive to the pretreatment of the catalysts and the reduction procedure (calcination temperature, heating rate and the mode and temperature profile of the temperature programmed reduction, TPR).[8,60] For details, we refer to our previous work,

where we summarized our TPR data obtained under the same experimental conditions:[29] The pure CeO$_2$ support (calcined at 973 K) displays an asymmetric low temperature feature with a rate maximum at 789 K (note that its intensity gradually decreased as TPR runs were repeated, indicating a reduction in the surface region). In addition, a pronounced high temperature peak was detected at 1090 K, attributed to the bulk reduction of the ceria support.[61] In agreement with literature data the reduction of Rh occurs up to 500 K.[61] In the present study, the peak maxima were observed at 403, 395 and 390 K for 0.1%, 1% and 5% Rh/ceria, respectively (not shown).

Upon adding 2% Co to CeO$_2$, the high temperature feature at 1090 K due to bulk reduction of ceria shows a slight increase, and an additional well-resolved doublet appeared, with peak maxima at 590 and 639 K. This characteristic reduction profile has been previously reported for Co/CeO$_2$,[25] and is consistent with a stepwise reduction scheme, first from Co$_3$O$_4$ to CoO and thereafter from CoO to metallic Co. The XPS results on 2% Co/CeO$_2$ (see below) indicated that the reduction of Co is not complete up to 773 K. When the Co loading was increased to 10%, the intensity of the low-temperature doublet increased and shifted to lower temperatures (563 and 626 K), and the peak at around 756 K significantly intensified.[29] Adding Rh (0.1–5%) to 2% Co supported on CeO$_2$ remarkably altered the TPR profile. The doublet moved to lower temperatures (479 and 574 K in the 0.1% Rh case), with the shift being more pronounced for the lower temperature peak, i.e., for the reduction of Co$_3$O$_4$ to CoO.[29]

In this present work, the highest reduction temperature applied in the SRE experiment is 773 K. This temperature is sufficient only for the surface reduction of ceria (and not the bulk); at the same time, the reduction of Rh is complete and only partial reduction of Co occurs.

The pretreated catalysts were tested in ethanol steam reforming (SRE). Fig. 1 displays the conversion of ethanol and
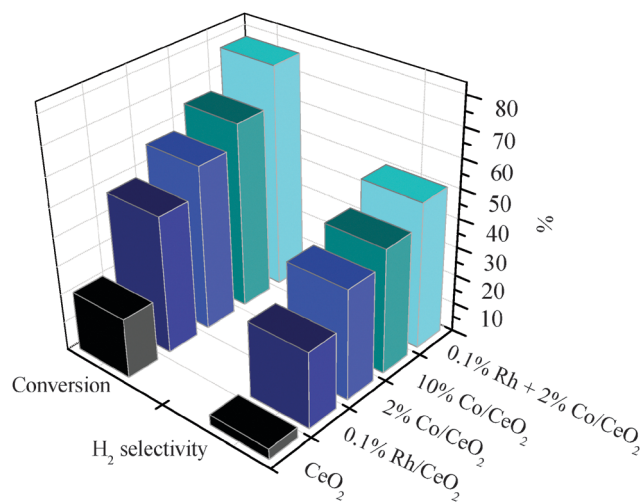

Fig. 1 Ethanol conversion and hydrogen selectivity in the EtOH + H$_2$O (1 : 3) reaction at 723 K on Co- and Rh-containing ceria based catalysts. Data are plotted at 120 min reaction time.

the hydrogen selectivity values obtained on 0.1% Rh/CeO$_2$, 2% Co/CeO$_2$, 10% Co/CeO$_2$ and 0.1% Rh + 2% Co/CeO$_2$, after 120 min reaction time at 723 K. For comparison we demonstrated the values measured on CeO$_2$ support, too. The highest values were obtained on the 0.1% Rh + 2% Co/CeO$_2$ catalyst. The figure clearly shows that the effect of 0.1% Rh is more significant than the increase in Co loading in terms of both conversion and selectivity. Notably the Rh promoted Co catalyst exhibited constant activity after 70 min of reaction time.[29]

3.2 Characterization by powder X-ray diffraction (XRD) and transmission electron microscopy (HRTEM)

The XRD patterns of ceria, Rh/ceria and Co/ceria catalysts after calcination and the oxidation/reduction process are shown in Fig. 2. In order to avoid or at least minimize re-oxidation, a glove box was used to transfer the samples from the preparation chamber to the XRD apparatus. The observed reflections (28.5° for (111), 33.0° for (200), 47.5° for (220), 56.3° for (311) and 59.1° for (222) facets of nearly stoichiometric ceria) agree well with the literature data of cubic CeO$_2$.[24,25,62,63] After pre-reduction at 773 K, the coordination number of Ce^{4+} to O^{2-} is reduced from eight to seven and Ce^{3+} ions are introduced into the crystal lattice. The Ce^{3+} ions have higher ionic radii than Ce^{4+} ions, and instead of the (111) lattice plane in pristine ceria, planes with higher Miller indexes became dominant because the formation of Ce^{3+} ions increased the lattice spacing.[11,64] This slight reduction can be detected by XPS, too (see below). Taking into account the peak broadening by the apparatus, the average size of the ceria crystallites was 27.6 nm, determined by Scherrer's method for the (111) reflection (Table 1).

When the ceria was loaded with Rh, nearly no change could be observed in the ceria diffraction pattern; only a new weak reflection appeared at 41.0°, which is identified as the Rh(111) plane (Fig. 2B). At 0.1% and 1% Rh, reflection from Rh could not be detected due to the small metal content and large dispersion. After zooming on into the diffractogram, the reflection at 41.0° for the Rh(111) plane is clearly visible for a Rh content of 5%. In addition, very small extra reflections are seen at 39.5° and 42.5°. The former originates from the sample holder, the latter is due to a ceria structure, which was identified to be different from the cubic structure. The XRD line shapes of ceria remained unchanged in the presence of Rh (Fig. 2A). For 5% Rh/ceria, where the XRD peak had sufficient intensity, we estimated the average crystallite size to be 6.0 nm, which is very close to the value determined by TEM (see below). It is known from the literature that the particle size determination from TEM images is not an easy task. Idriss et al.[65] reported that TEM did not show conclusive evidence for the presence of metals on a CeO$_2$ support. From the other work, it can be inferred that the surface area of ceria influenced the size of Rh particles. At 1% Rh content on a low surface area material (14 m^2 g^{-1}), where coarse CeO$_2$ grains are observed, the size of Rh clusters falls in the 5–20 nm range; on a high surface area CeO$_2$ support (275 m^2 g^{-1}), the size varied from 4 to 8 nm.[66]

In our case, the surface areas of the supported catalysts were 19.8–17 m^2 g^{-1} (Table 1), depending on the Rh content

This journal is © the Owner Societies 2015

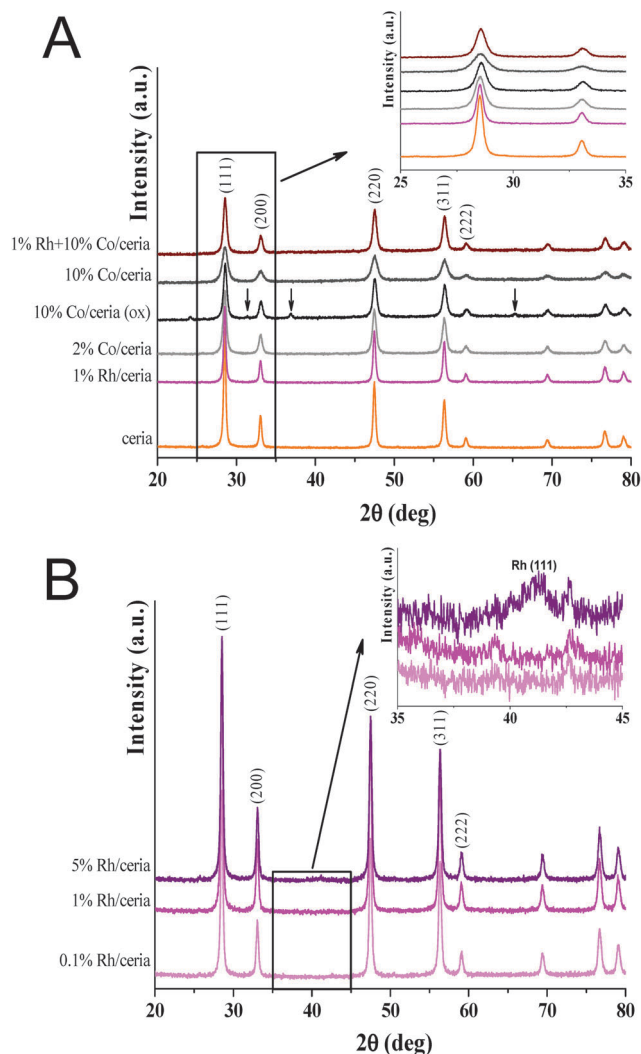Phys. Chem. Chem. Phys., 2015, 17, 27154–27166 | 27157

Fig. 2 XRD patterns of different ceria and ceria supported Rh, Co and Rh–Co catalysts. The insets show the zoomed area of (111) and (200) reflections of CeO2 (A) and Rh(111) (B).

Fig. 3 TEM images of ceria and ceria supported Rh, Co and Rh–Co catalysts.

(0.1–5%). The Rh particle size varied between 2.4–6.5 nm on 1% Rh/ceria and on 5% Rh/ceria. In the latter case, a small portion of the particles was around 10 nm in size. The typical HRTEM images are shown in Fig. 3. For 0.1% Rh/ceria, the particle size determination was ambiguous due to the very low content and high dispersion. It is important to note that the Rh loading did not alter the ceria particle sizes (Table 1).

The XRD patterns of Co-containing ceria (2% and 10%) are also presented in Fig. 2. On oxidized Co-containing samples, apart from the ceria reflections very weak extra reflections appeared, which are attributed to Co_3O_4 (31.5° for (220), 36.9° for (311) and 65.2° for (400)). The average crystallite size of Co_3O_4 was calculated to be 22.5 nm from the (311) reflection. In contrast to the oxidized catalysts, Co_3O_4, CoO and Co phases are very difficult to observe on the reduced catalysts. In the literature, only a very weak reflection was reported at 44° for metallic Co at a similar reduction temperature, even for 10% Co content in ceria.[25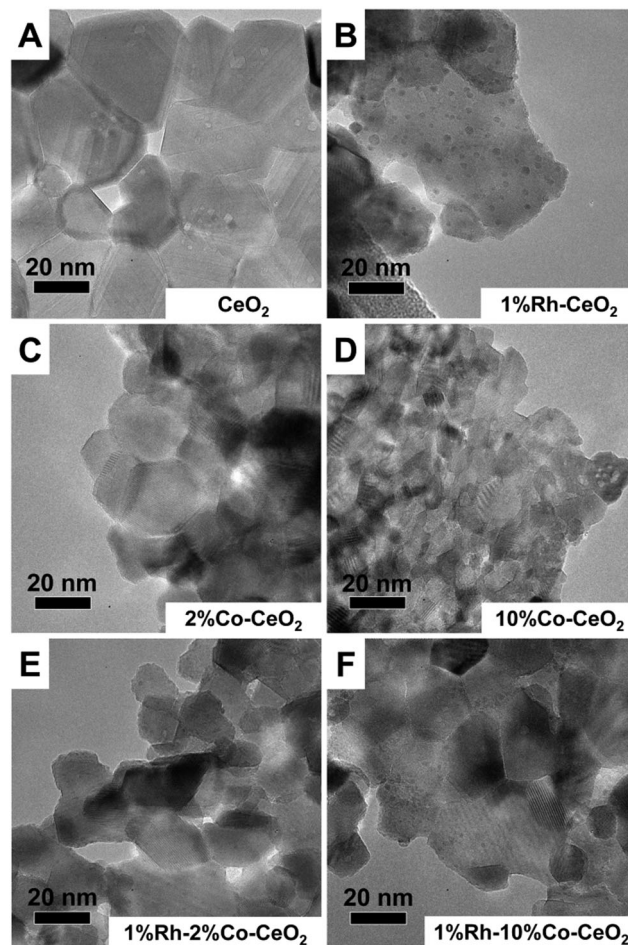] The lack of Co^{2+} or Co reflections can be explained by a significant dissolution of Co into ceria. Our previous XPS and LEIS work on a Co/CeO_2(111) model catalyst demonstrated that above 750 K Co significantly penetrated into the ceria support.[39] Notably, the ceria peak positions do not change due to Co-loading; however, at the same time, the peaks significantly broadened, particularly at 10% Co content (Fig. 2A). This behavior, in agreement with the HRTEM images (Fig. 3C and D), indicates that the presence of Co induces a disruption process in the ceria phase. Calculations using Scherrer's method for the (111) reflection of CeO_2 show that the ceria crystallite size became smaller, 17.1 nm for 2% Co/ceria, and 10.7 nm for the 10% Co/ceria catalyst (Table 1). While the high temperature hydrogen treatments (reduction) play an important role in the disruption phenomenon, the oxidation step did not cause such a dramatic effect: for the 10% Co/ceria catalyst, the ceria particle size decreased from 27.6 to 16.9 nm upon oxidation of the calcined Co-containing sample at 673 K. In agreement with a literature observation,[63] Co-oxides and metallic Co particles are difficult to distinguish in HRTEM from the CeO_2 particles, due to the low contrast and the above mentioned significant dissolution.

For the Rh–Co bimetallic cases, a similar broadening of the ceria reflections takes place, though to a lesser extent than for

Co/ceria samples (Fig. 2A). In the case of 1% Rh + 10% Co/ceria, the ceria particle size was calculated to be 17.1 nm; the respective value without Rh was 10.7 nm. This behavior indicates that this small amount of Rh may inhibit the Co-induced disruption of ceria. A similar moderate change was observed for 1% Rh + 2% Co/ceria (Table 1). It is important to note that new reflections were not observed for the bimetallic system.

3.3 CO adsorption on Rh/ceria and Co–Rh/ceria, DRIFTS experiments

The morphology of Rh supported on CeO_2 was also investigated by FTIR, employing adsorbed CO as a probe molecule, which is sensitive to the local surface structure (Fig. 4). Adsorbed CO exhibits at least three different $\nu(C\equiv O)$ stretching frequencies

belonging to certain adsorption sites on oxide-supported Rh.[15,67,68] The band at 2070–2030 cm^{-1} is due to CO adsorbed linearly to Rh^0 (depending on the CO coverage). Bridge-bonded CO (Rh_2–CO) exhibits a band at $\sim$1855 cm^{-1} (not shown) and a pair of peaks at $\sim$2100 and $\sim$2020 cm^{-1} corresponds to the asymmetric and symmetric stretching of $Rh^+(CO)_2$ (twin CO). These latter IR signals were detected when the oxide is covered by atomically dispersed Rh or when the crystallite size of Rh was very small.[67] The linear mode develops on bigger particles.

The samples were reduced at 773 K prior to CO adsorption. The adsorption of CO was performed in a flow system using 10% CO in He at room temperature for 30 minutes. Afterward, the reactor was flushed with He for 30 minutes and the sample was heated in He flow with a heating rate of 20 K min^{-1}. Fig. 4A
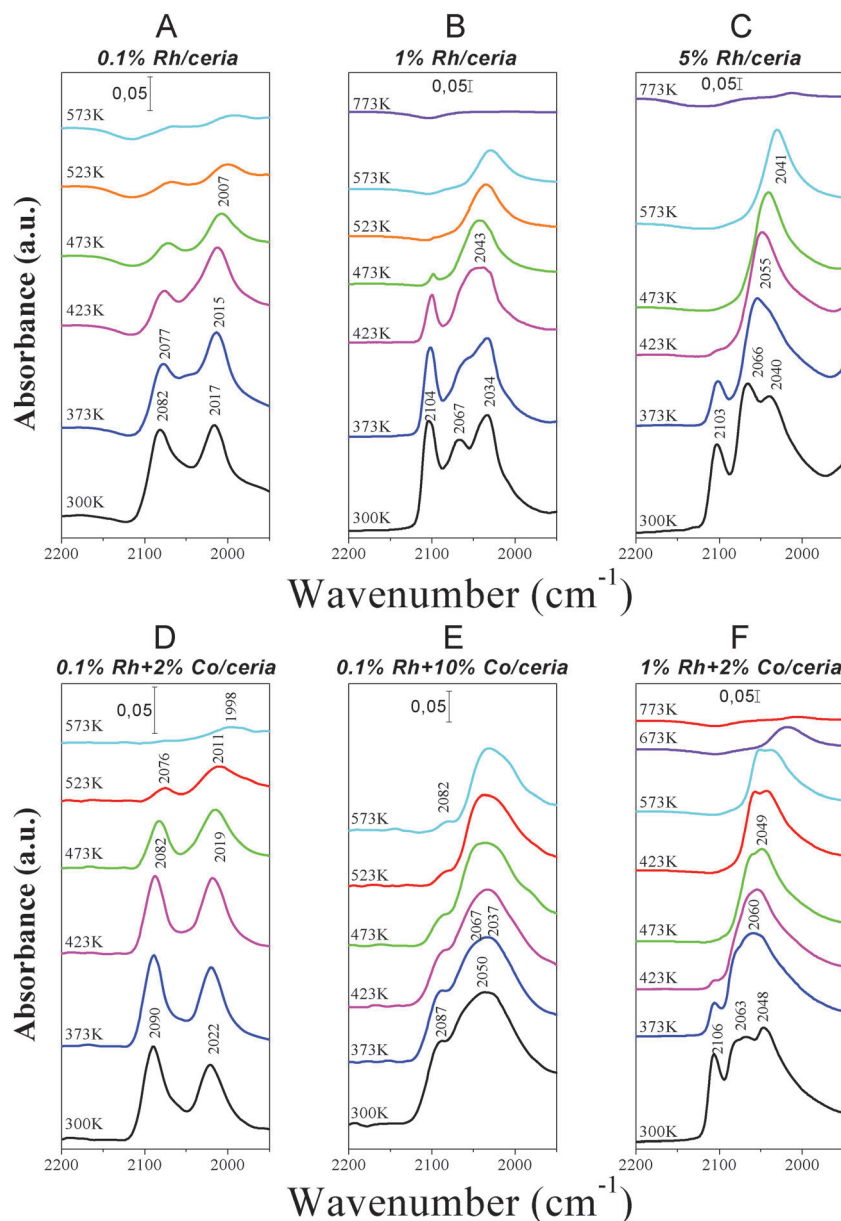

Fig. 4 DRIFT spectra after CO adsorption (at 300 K) followed by subsequent annealing at higher temperatures on (A) 0.1% Rh/ceria, (B) 1% Rh/ceria, (C) 5% Rh/ceria, (D) 0.1% Rh + 2% Co/ceria, (E) 0.1% Rh + 10% Co/ceria and (F) 1% Rh + 2% Co/ceria.

This journal is © the Owner Societies 2015

Phys. Chem. Chem. Phys., 2015, 17, 27154–27166 | 27159

represents spectra obtained on 0.1% Rh/ceria. At 300 K, two bands with almost equal intensity were observed at 2082 and 2017 cm^{-1}, which can be attributed to a dicarbonyl Rh species associated with Rh$^+$ ions.[15,67,69] A similar Rh twin dicarbonyl feature was obtained on Rh/alumina catalysts at very low metal content with high dispersity.[67] Upon increasing the temperature to 373 K, the intensity between the twin peaks, that is around 2050 cm^{-1}, increased, which is attributed to the development/increase of the linear species. At the same time, the twin peaks shifted to lower wavenumbers and lost intensity, in harmony with the literature.[69,70] These changes occur in connection with the desorption of CO and the agglomeration of Rh particles. At 1% and 5% Rh content (Fig. 4B and 3C, respectively), the FTIR spectra contain the bands of the dicarbonyl species and the linearly bonded CO mode at 2067 cm^{-1} at 300 K, indicating the presence of larger Rh crystallites already at this temperature. Upon annealing, the twin dicarbonyl form is transformed into the linear mode, which has higher thermal stability. It desorbs above 673 K.

Next, we discuss the influence of co-adsorbed Co. On the 0.1% Rh + 2% Co/ceria catalyst, similar to the Co-free surface, the twin peaks of the Rh twin dicarbonyl species were detected at 300 K. The ν_{as}(C≡O) peak at 2090 cm^{-1} was even sharper and less asymmetric than in the Co-free case, indicating the almost complete absence of linearly bonded CO. The DRIFT spectra were dominated by the twin feature also at higher temperatures, with stepwise decreasing intensities (Fig. 4D). In other words, 2% Co stabilized the small Rh particles when Rh was present in trace amounts. A different behavior was detected for 10% Co content (Fig. 4E), where already at 300 K, besides the small fraction of dicarbonyl species, a strong broad band appeared at around 2050 cm^{-1}. Very probably, it is composed of (at least) two peaks (~2067 and ~2037 cm^{-1}), which are tentatively assigned to CO bound linearly to metallic Rh and Co, respectively. We note that in separate experiments on Rh-free Co-containing samples a very weak band appeared at 2037 cm^{-1} (not shown) that is attributed to CO bonded to a metallic fraction of cobalt, since CO cannot adsorb on oxidized Co at 300 K. The appearance of linearly bonded CO on Rh thus indicates that the higher Co loading induces some agglomeration of Rh for 0.1% Rh + 10% Co/ceria. For 1% Rh + 2% Co/ceria (Fig. 4F), the two adsorption modes of CO, linearly bonded to Rh (2063 cm^{-1}) and Co (2048 cm^{-1}) can be clearly distinguished. A different DRIFT feature was observed on the MgO supported Co–Rh bimetallic system.[71] Only linearly bonded CO species was detected. The position of the linear CO band on Rh–Co/MgO was located between those on Rh/MgO and Co/MgO, and the linear CO band on Rh–Co/MgO was much broader than that of Rh/MgO. This may suggest the formation of a well-mixed Rh–Co alloy, which was also verified by the Rh K- and Co K-edge EXAFS analysis.[31,72] In our ceria supported bimetallic system similar univoque conclusion could not be deduced from DRIFTS measurements. Although the strong broadening in the linear CO range – especially in the case of 0.1% Rh + 10% Co/ceria – may indicate a certain extent of alloy formation.

3.4 X-ray photoelectron spectroscopy

Fig. 5 shows the Rh 3d spectra of 0.1% Rh/ceria (A), 1% Rh/ceria (B) and of 5% Rh/ceria (C and D) after oxidation and reduction followed by stepwise heating in inert gas. After oxidation at 673 K, on all three samples the Rh 3d$_{5/2}$ peak appeared at 309.2 eV and the Rh 3d$_{3/2}$ peak at 314.0 eV. After reduction at 773 K, the doublet markedly decreased in intensity and shifted to lower binding energies; the Rh 3d$_{5/2}$ component at 307.1 eV indicates a metallic state. The drastic intensity decrease may be attributed to the agglomeration (sintering) and perhaps to some encapsulation of Rh particles by the ceria support. We note that the total amount of Rh did not change, as shown by our EDX measurements. The agglomeration of Rh is also evidenced by TEM images, which show an increase of the average size from 1.1 ± 0.45 nm before reduction to 3.9 ± 1.45 nm after reduction on 1% Rh/ceria. A similar drastic increase was obtained on 5% Rh/ceria, from 1.3 ± 0.3 to 4.7 ± 2.0 nm. The agglomeration is
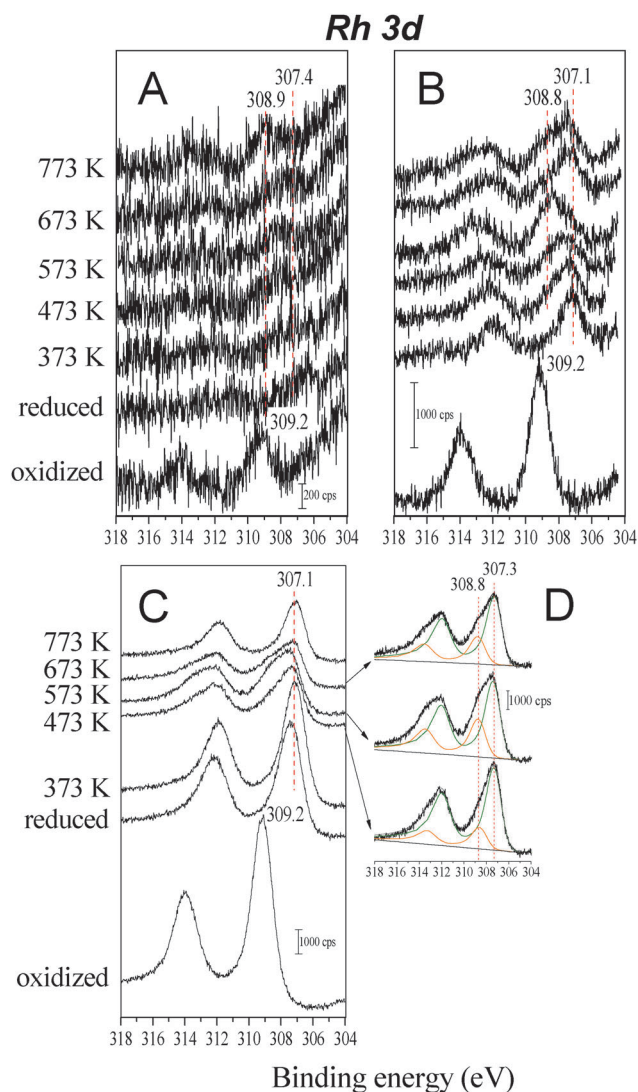

Fig. 5 Rh 3d XPS after oxidation (673 K), reduction (773 K) and subsequent heating in a nitrogen atmosphere; (A) 0.1% Rh/ceria, (B) 1% Rh/ceria, (C) 5% Rh/ceria and (D) deconvoluted spectra of (C).

27160 | *Phys. Chem. Chem. Phys.*, 2015, **17**, 27154–27166

This journal is © the Owner Societies 2015

frequently attributed to Ostwald ripening; in this scenario, the mass transport is realized by the migration of individual atoms that are detached from the clusters. An alternative way would be coalescence by cluster migration, which was demonstrated by STM for small clusters ($\sim$10 atoms) on Pd/TiO$_2$(110) even at room temperature.[73] Encapsulation of Rh is well-documented on TiO$_2$(110) above 700 K, as shown by XPS, LEIS and STM.[74,75] Partial covering by ceria was observed recently on the Rh–CeO$_2$/MgO system by using the DRIFTS method.[71] Very recently, near ambient pressure X-ray photoelectron spectroscopy (nap-XPS) demonstrated that the strong metal support interaction effect (SMSI) found in the Ni–ceria system is associated with the decoration and burial of metallic particles by the partially reduced support.[76] We cannot exclude that this process occurs in the Rh–ceria system; however, since CO adsorption is not blocked after reduction (see the DRIFTS results), encapsulation is probably very limited, if any, below 773 K.

After reduction, the samples were heated in a nitrogen atmosphere in the catalysis chamber from 300 to 773 K, and were held at that temperature for 2 min. Upon heating, we find a broadening of the Rh 3d feature for all Rh loadings, indicating the appearance of a new component at 308.8 eV (Fig. 5). The changes can be better analyzed for the higher Rh loadings of 1% and 5% Rh (5B and 5C), respectively, and some additional representative data for lower metal content are included in Fig. S2 (ESI†). On the oxidized samples, the Rh 3d$_{5/2}$ peak is observed at 309.2 eV, after reduction it shifted to 307.1 eV. Upon heating, a shoulder developed at 308.8 eV and reached maximum intensity at 573 K and then decreased again at higher temperatures. At 773 K the main peak was situated at 307.1 eV and a shoulder remained at 308.8 eV. In Fig. 5D, the spectra of the 5% Rh/ceria catalyst obtained at 473, 573 and 673 K (Fig. 5C) are deconvoluted, showing two well separated peaks at 307.3 and 308.8 eV.

Basically, we may consider two reasons for the upward shift of the Rh 3d peaks. One explanation could be an electronic interaction between Rh and ceria, which was observed between reduced titania and different metals including Rh.[77–80] The presence of a high number of defects and oxygen vacancies in ceria or in titania could initiate an increased electron flow between the metal and the support. Recently, TiO$_2$(110) surfaces with Pt adatoms were examined using a noncontact atomic force microscope (NC-AFM) and a Kelvin probe force microscope (KPFM). The observed work function decrease was attributed to an electric dipole moment directed toward the vacuum, as a result of electron transfer from the adatom to the TiO$_2$ substrate.[81,82] Similar phenomena may occur for the Rh–ceria system, forming partially positively charged Rh. The second possibility could be an oxygen transport from ceria to Rh, causing the observed shift in the Rh 3d spectra. Earlier, oxygen migration was supported by TPD and Auger spectroscopy for the Rh–ceria system,[83,84] and recently an STM study gave further evidence.[85] Moreover, Vayssilov et al.[13] showed the coexistence of two different interaction mechanisms, a purely electronic effect involving electron transfer from Pt to CeO$_2$ and a second channel, involving transport of activated oxygen from

nanostructured ceria to Pt, i.e. oxygen spillover. Both effects were experimentally detected using resonant photoelectron spectroscopy. In our case, the oxygen migration from ceria to Rh is detectable above 373 K in XPS (Fig. 5), and is most pronounced between 473–673 K. Interestingly, the oxygen spillover is partially reversible, as indicated by the dominance of the metallic Rh peak at 773 K. The easy formation of this Rh–O species and its stability–instability on ceria may be responsible for the strongly enhanced catalytic activity of Rh in several catalytic reactions.

In an alternative explanation of our XPS data, we may also suppose the formation of Rh–O–Ce and Rh–O–Rh bonds which were demonstrated earlier by in situ quick scanning X-ray absorption fine structure (QXAFS) experiments.[86] Oxidation and reduction of Rh species on Rh/CeO$_2$/SiO$_2$ catalysts were promoted by the presence of CeO$_2$ as indicated by the comparison of the profiles of the temperature-programmed oxidation (TPO) and reduction (TPR) of Rh/CeO$_2$/SiO$_2$.[86] In situ QXAFS during the TPO and TPR indicated that the formation of the Rh–O–Ce bond was followed by that of Rh–O–Rh during the TPO.

From Fig. 6A, it is evident that the source of the oxygen is the ceria itself. We note here that the XP spectra of ceria is rather complex, it was analyzed after literature. A minor reduction of Ce^{4+} to Ce^{3+} is best detectable as the small intensity increase of the u′ (903.9 eV) and v′ (885.3 eV) peaks and also the weaker u^0 (899.3 eV) and v^0 (880.2 eV) components, which are characteristic of Ce^{3+}.[28,29,87–89] As Fig. 6A shows, the Ce^{3+}/(Ce^{4+} + Ce^{3+}) ratio is higher on the Rh/ceria system than on reduced ceria (compare the bottom and center spectrum). Notably, the increase is smaller than expected. The reason is that above 373 K the diffusion of bulk oxygen to the surface is very quick as it was observed in a separate experiment shown in Fig. 6B. Therein, CeO$_2$ was first strongly reduced (Ce^{3+} signal indicated by a vertical arrow), and subsequently stepwise heated in a vacuum; at each temperature the sample was kept for 2 min. The figure shows that above 473 K the ceria surface significantly re-oxidized with oxygen provided by the ceria bulk as a reservoir.

In Fig. 7 we display the Co 2p$_{3/2}$ spectra from the 2% Co/ceria and 10% Co/ceria samples. After oxidation at 673 K, the characteristic signal from Co$_3$O$_4$ appeared at 779.7 eV. Upon reduction at 773 K, the intensity of the Co peak decreased and only a small new peak characteristic of metallic Co developed at 777.8 eV; this indicates that Co is difficult to reduce at this temperature.[21,24,28,29] The overall intensity decrease may be attributed to the dissolution in ceria and encapsulation of cobalt clusters by the support. Agglomeration or coalescence did not play a significant role, because the Co XP peaks gained intensity when the sample temperature was increased in stepwise manner after evacuation in a nitrogen atmosphere (Fig. 7A and B). The other remarkable change during the heat treatment is the disappearance of the metallic Co peak at 777.8 eV above 473 K, marking the significant oxidation of cobalt to Co^{2+}. Although the Co 2p$_{3/2}$ peak positions of CoO and Co$_3$O$_4$ are almost the same, the presence of CoO (Co^{2+}) is indicated by the characteristic satellite at higher binding energies (compare the

This journal is © the Owner Societies 2015

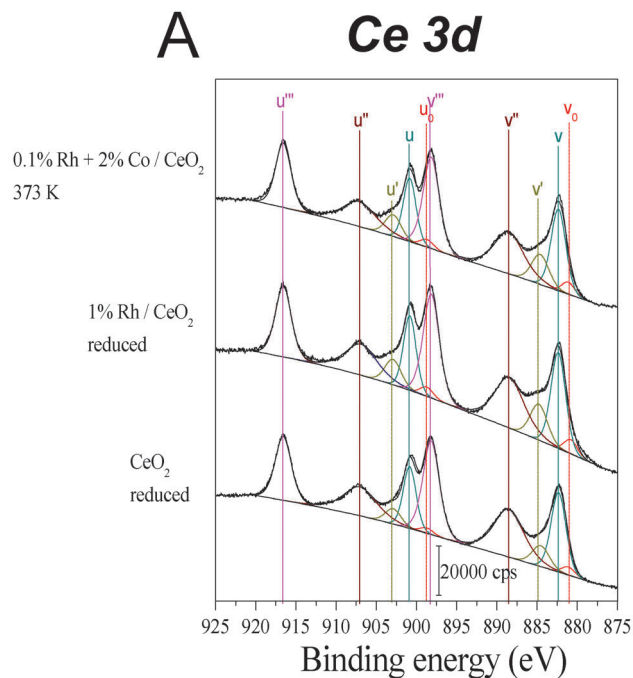Phys. Chem. Chem. Phys., 2015, **17**, 27154–27166 | **27161**

Fig. 6 Ce 3d XP spectra obtained on reduced ceria and Rh, Rh–Co containing ceria (A). Strongly reduced (at 773 K for 120 min) ceria heated in a vacuum at different temperatures (B).
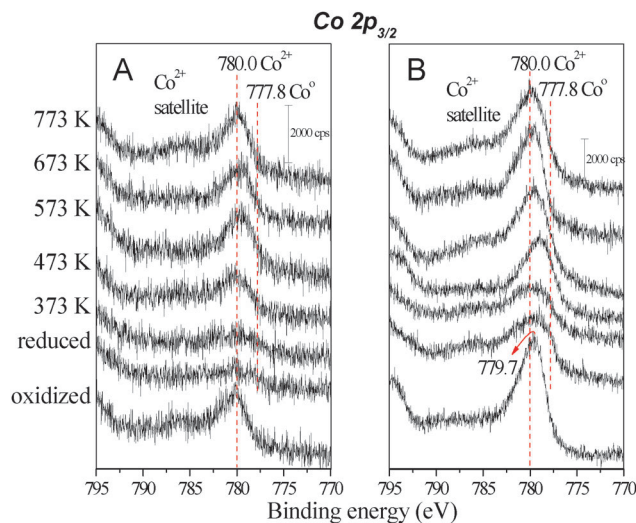

Fig. 7 Co $2p_{3/2}$ XP spectra obtained on 2% Co/ceria (A) and 10% Co/ceria catalysts (B) after oxidation and reduction and subsequent heating under inert gas.

(ESI†). In the Co–ceria system, the decrease of Co XPS signal upon hydrogen reduction is attributed to the encapsulation by ceria as was also found for the Ni/ceria system.[76] It is interesting that this process is reversible, which is concluded from the fact that CoO is recovered above 473 K. In this sense, the Co/ceria system is close to the Ni/ceria catalyst, where the hydrogen-induced burial (encapsulation) and dig out of Ni is a reversible process.[76]

The spectra of the monometallic Rh–ceria or Co–ceria systems were significantly altered in the presence of the second metal. Fig. 8 displays the Rh 3d and Co $2p_{3/2}$ spectra obtained after oxidation/reduction and subsequent heat treatment at different temperatures for the 0.1% Rh + 2% Co/ceria and 0.1% Rh + 10% Co/ceria catalysts. When comparing the Rh 3d signals of the monometallic 0.1% Rh system (Fig. 5A) and the bimetallic Rh–Co systems (Fig. 8A and B), the first important observation is the significantly higher intensity for the latter. This behavior indicates that a larger fraction of Rh is accessible for XPS even after reduction, due to a suppression of agglomeration or encapsulation in the presence of Co adatoms. Notably, this was concluded from the DRIFTS measurement, too (Fig. 4A and D). The inhibited agglomeration of Rh in the presence of Co is also clearly evident from the HRTEM images for 1% Rh + 2% Co/ceria before and after reduction. The particle sizes did not alter after reduction at 773 K. 1.5 ± 0.5 nm was measured before reduction and 1.7 ± 0.6 nm was obtained after reduction. Very similar data were obtained for 1% Rh + 10% Co/ceria. For comparison we mention again that the reduction of monometallic 1% Rh/ceria resulted in 2.4–6.5 nm particle sizes. Fig. 3E and F represent HRTEM images of reduced bimetallic systems showing the inhibiting effect of Co on Rh agglomeration.

Based on the XRD, TEM and DRIFTS results, we should distinguish between the 2 and 10% Co-containing catalysts in the interpretation of XPS results for the bimetallic Rh–Co

top and bottom spectrum in Fig. 7B) and the spin–orbit splitting of 16.0 eV. This high value is typical for paramagnetic Co^{2+} compounds due to multiplet splitting. After oxidation (Fig. 7B top spectrum), the separation was only 15.2 eV close to the values on diamagnetic Co compounds like Co^{3+} complexes.[90,91] Peak fittings of some Co 2p spectra are depicted in Fig. S2

27162 | Phys. Chem. Chem. Phys., 2015, 17, 27154–27166
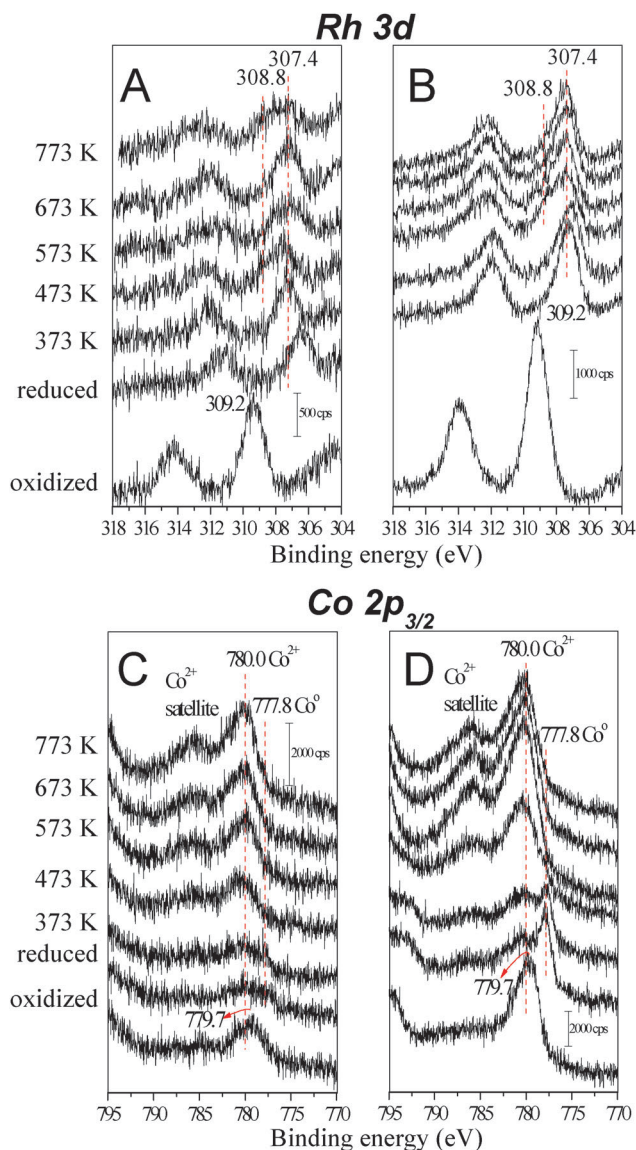
This journal is © the Owner Societies 2015

Fig. 8 Rh 3d XP spectra obtained on Rh–Co bimetallic catalysts: 0.1% Rh + 2% Co/ceria (A) and 0.1% Rh + 10% Co/ceria (B). Co $2p_{3/2}$ XP spectra obtained on Rh–Co bimetallic catalysts: 0.1% Rh + 2% Co/ceria (C) and 0.1% Rh + 10% Co/ceria (D).

system. As presented above, 2 and 10% Co loading results in a drastic increase of the ceria dispersion; this effect is much more pronounced at 10% Co loading (Fig. 2A, Fig. 3C and D). Our DRIFTS results (Fig. 4D) demonstrated that 2% Co stabilizes a higher dispersion of Rh, and 10% Co increases the formation of larger particles; nevertheless, the significant intensity from twin-dicarbonyl species after CO adsorption indicates that nearly atomically dispersed Rh is still present up to 473–523 K. We therefore conclude that Rh agglomeration is probably hindered in the bimetallic system at low Co content of 2%, but slightly occurs at the higher content of 10% Co.

Another significant observation is that for the bimetallic Rh–Co system, the Rh 3d peak at ∼308.8 eV due to oxygen migration above 300 K is less pronounced than for the

monometallic system (compare Fig. 5, Fig. 8A and B). This indicates that such kind of oxygen transport occurs in the bimetallic system, but to a lesser extent than for the mono-metallic case. It also seems that Co delays the oxygen migration from ceria to Rh.

Fig. 7C and D display the Co $2p_{3/2}$ region after reduction and following heat treatment. It is remarkable that mainly at 10% Co content the presence of Rh significantly assisted the reduction of Co^{2+} to Co^0, as was experienced in our previous work.[29] Upon thermal treatment, Co $2p_{3/2}$ moved to higher binding energy from 777.8 eV to 780.0 eV indicating the re-oxidation of metallic Co. Above 473 K, the re-oxidation to mainly Co^{2+} is completed (Fig. 8A and B). As it can be seen in Fig. 6A, the ceria is in a slightly reduced state in the bimetallic system, too. It is very important to note that compared to the monometallic Rh sample, the oxygen migration from ceria to Rh is less pronounced in the presence of Co adatoms. In the bimetallic system, the Co oxidation by ceria is faster than the oxygen migration from ceria to Rh. Highly dispersed metallic Rh can facilitate the reduction of Co^{2+} and the formed metallic Co can be rapidly re-oxidized by the ceria.

3.5 Low-energy ion scattering (LEIS) experiments

As LEIS is widely used to determine the outermost surface composition[92] we also tried to map the top layer of the Rh/ceria system. This method was successfully applied in our previous studies even for porous materials (titania-supported Au and Rh).[52] In spite of this fact, unfortunately, this method some-times is far from straightforward. In certain cases, neutraliza-tion effects can be too strong. This enhanced neutralization was experienced for Ce/Rh(111)[93] and to a certain extent on Ce/Cu(111), when Ne^+ was used.[58] In our extended LEIS experi-ments on the Rh/ceria system a Rh signal was not detected. We suppose that a strong neutralization effect could be the reason for the lack of Rh signals in LEIS in the present cases, although we have learnt from DRIFTS experiments using CO adsorption that a certain amount of Rh should exist on the surface. The Rh LEIS signal was not detected even after prolonged etching with 4 keV ions.

Next, we studied the surface composition of the Co/ceria system using the LEIS technique applying 800 eV He^+ ions (Fig. 9). For comparison, we display a LEIS spectrum of a clean CoO standard. After reduction of 10% Co/ceria, the Co signal was very weak. The almost complete lack of the Co signal can be explained mostly by the penetration or dissolution of cobalt into the ceria and to a lesser extent by encapsulation by ceria. A similar conclusion was drawn from XRD and XPS experiments (see above). Our recent XPS and LEIS work on a $Co/CeO_2(111)$ model catalyst demonstrated that Co^{2+} penetration into the ceria layer was significant and that for metallic Co presumably agglomeration occurs.[39] It was verified that no disturbing neutralization effects occur for the Co peaks in LEIS using He^+ or Ne^+ projectiles; however, since strong matrix effects are found for the O peak with He^+, this peak was not used for quantitative analysis.

This journal is © the Owner Societies 2015
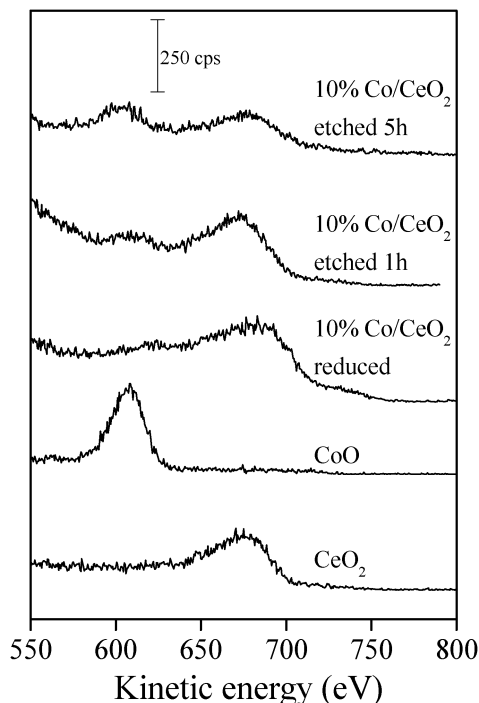
Phys. Chem. Chem. Phys., 2015, 17, 27154–27166 | 27163

Fig. 9 LEIS spectra of reduced ceria, clean CoO standard, reduced 10% Co/ceria and etched Co/ceria obtained with 800 eV He⁺.

If encapsulation or dissolution phenomena would be the main cause for the lack of a Co signal in Co/ceria catalysts, we should detect a Co signal after prolonged Ar⁺ or Ne⁺ ion bombardment. As Fig. 9 demonstrates, Co indeed showed up, with its intensity increasing with etching time.

4. Summary and conclusion

We investigated CeO_2-supported Rh, Co and bimetallic Rh–Co catalytic materials using XRD, HRTEM, DRIFTS, XPS and LEIS. Our studies concentrated mainly on the reduced materials, which successfully operate under real catalytic conditions.

1. At small Rh loading (0.1%), Rh is in a very dispersed state on ceria, while at higher Rh loadings (1–5%), Rh forms 2–8 nm particles. HRTEM and XPS showed significant agglomeration at a high temperature (773 K). DRIFTS using CO adsorption showed that the encapsulation does not fully occur, and some atomically dispersed Rh may exist even after high temperature reduction.

2. On reduced Rh/ceria, oxygen transfer from ceria to Rh and possibly also electron transfer from Rh to ceria take place, according to XPS. Oxygen transport from ceria to Rh is well-detectable between 473 and 673 K.

3. XRD and HRTEM revealed that loading with Co induces the formation of smaller ceria crystallites; for 10% Co/ceria, the CeO_2 particle size decreased from 27.6 to 10.7 nm. Co is almost completely oxidized to Co^{2+}.

4. Strong dissolution of Co into ceria and a certain extent of Co encapsulation by ceria were experienced by XRD, XPS and LEIS.

5. The presence of Rh adatoms enhances the reduction of cobalt. During thermal treatment, re-oxidation of Co takes place in the bimetallic system. The Rh agglomeration and oxygen migration from ceria to Rh are hindered by the presence of cobalt. Ceria is in a slightly reduced state on Rh/ceria, Co/ceria and on the bimetallic materials.

Author contributions

The manuscript was written through contributions of all authors. All authors have given approval to the final version of the manuscript.

Conflicts of interest

The authors declare no competing financial interest.

Acknowledgements

References

1 G. W. Huber, S. Iborra and A. Corma, *Chem. Rev.*, 2006, **106**, 4044–4098.

2 M. Balat, *Int. J. Hydrogen Energy*, 2008, **33**, 4013–4029.

3 D. Chen and L. He, *ChemCatChem*, 2011, **3**, 490–511.

4 L. F. Brown, *Int. J. Hydrogen Energy*, 2001, **26**, 381–397.

5 A. Haryanto, S. Fernando, N. Murali and S. Adhikari, *Energy Fuels*, 2005, **19**, 2098–2106.

6 R. D. Cortright, R. R. Davda and J. A. Dumesic, *Nature*, 2002, **418**, 964–967.

7 Y. Lykhach, A. Neitzel, K. Sevcikova, V. Johánek, N. Tsud, T. Skála, K. C. Prince, V. Matolin and J. Libuda, *ChemSusChem*, 2014, **7**, 77–81.

8 A. Trovarelli and P. Fomasiero, *Catalysis by Ceria and Related Materials*, Imperial College Press, London, 2nd edn, 2013.

9 S. D. Park, J. M. Vohs and R. J. Gorte, *Nature*, 2000, **404**, 265–267.

10 G. A. Deluga, J. R. Salge, L. D. Schmidt and X. E. Verykios, *Science*, 2004, **303**, 993–997.

11 C. T. Campbell and C. H. F. Peden, *Science*, 2005, **309**, 713–714.

12 L. V. Mattos, G. Jacobs, B. H. Davis and F. B. Noronha, *Chem. Rev.*, 2012, **112**, 4094–4123.

13 G. N. Vayssilov, Y. Lykhach, A. Migani, T. Staudt, G. P. Petrova, N. Tsud, T. Skála, F. Bruix, F. Illas, K. C. Prince, V. Matolin, K. M. Neyman and J. Libuda, *Nat. Mater.*, 2011, **10**, 310–315.

14 M. Mavrakis and M. A. Barteau, *J. Mol. Catal. A: Chem.*, 1998, **131**, 135–147.

15 A. Yee, S. J. Morrison and H. Idriss, *Catal. Today*, 2000, **63**, 327–335.

27164 | *Phys. Chem. Chem. Phys.*, 2015, **17**, 27154–27166

This journal is © the Owner Societies 2015

16 A. Erdőhelyi, J. Raskó, T. Kecskés, M. Tóth, M. Dömök and K. Baán, *Catal. Today*, 2006, **116**, 367–376.

17 J. Llorca, N. Homs, J. Sales and P. R. de la Piscina, *J. Catal.*, 2002, **209**, 306–317.

18 S. S. Y. Lin, D. H. Kim and S. Y. Ha, *Catal. Lett.*, 2008, **122**, 295–301.

19 J. Llorca, N. Homs and P. R. de la Piscina, *J. Catal.*, 2004, **227**, 556–560.

20 E. Martono, M. P. Hyman and J. M. Vohs, *Phys. Chem. Chem. Phys.*, 2011, **13**, 9880–9886.

21 E. Martono and J. M. Vohs, *J. Catal.*, 2012, **291**, 79–86.

22 M. S. Batista, R. K. S. Santos, E. M. Assaf, J. M. Assaf and E. A. Ticinalli, *J. Power Sources*, 2003, **124**, 99–103.

23 J. Kaspar, P. Fornasiero and M. Graziani, *Catal. Today*, 1999, **50**, 285–298.

24 H. Song and U. S. Ozkan, *J. Mol. Catal. A: Chem.*, 2010, **318**, 21–29.

25 B. Bayram, I. I. Soykal, D. Deak, J. T. Miller and U. S. Ozkan, *J. Catal.*, 2011, **284**, 77–89.

26 I. I. Soykal, H. Sohn and U. S. Ozkan, *ACS Catal.*, 2012, **2**, 2335–2348.

27 A. M. da Silva, K. R. Souza, L. V. Mattos, G. Jacobs, B. H. Davis and F. B. Noronha, *Catal. Today*, 2011, **164**, 234–239.

28 L. Óvári, S. Krick Calderon, Y. Lykhach, J. Libuda, A. Erdőhelyi, C. Papp, J. Kiss and H.-P. Steinrück, *J. Catal.*, 2013, **307**, 132–139.

29 Zs. Ferencz, A. Erdőhelyi, K. Baán, A. Oszkó, L. Óvári, Z. Kónya, C. Papp, H.-P. Steinrück and J. Kiss, *ACS Catal.*, 2014, **4**, 1205–1218.

30 E. Varga, Zs. Ferencz, A. Oszkó, A. Erdőhelyi and J. Kiss, *J. Mol. Catal. A: Chem.*, 2015, **397**, 127–133.

31 S. Naito, H. Tanaka, S. Kado, M. Toshihiro, S. Naito, K. Okumura, K. Kunimori and K. Tomishige, *J. Catal.*, 2008, **259**, 138–146.

32 H. Tanaka, R. Kaino, Y. Nakagawa and K. Tomishige, *Appl. Catal., A*, 2010, **378**, 187–194.

33 Y. Mukainakano, B. Li, S. Kado, T. Miyazawa, K. Okumura, T. Miyao, S. Naito, K. Kumimori and K. Tomishigi, *Appl. Catal., A*, 2007, **318**, 252–264.

34 Y. Mukainakano, K. Yoshida, K. Okumura, K. Kumimori and K. Tomishigi, *Catal. Today*, 2008, **132**, 101–108.

35 D. Li, Y. Nakagawa and K. Tomishigi, *Appl. Catal., A*, 2011, **408**, 1–24.

36 Zs. Ferencz, K. Baán, A. Oszkó, Z. Kónya, T. Kecskés and A. Erdőhelyi, *Catal. Today*, 2014, **228**, 123–130.

37 I. I. Soykal, H. Sohn, D. Singh, J. T. Miller and U. S. Ozkan, *ACS Catal.*, 2014, **4**, 585–592.

38 S. H. Overbury, D. R. Mullins and L. Kundakovic, *Surf. Sci.*, 2001, **470**, 243–254.

39 G. Vári, L. Óvári, J. Kiss, C. Papp, H.-P. Steinrück and Z. Kónya, *J. Phys. Chem. C*, 2015, **119**, 9324–9333.

40 K. M. Cook, S. Poudyal, J. T. Miller, C. Bartholomew and W. C. Hecker, *Appl. Catal., A*, 2012, **449**, 69–80.

41 G. Jacobs, Y. Ji, B. H. Davis, D. Cronauer, A. J. Kropf and C. L. Marshall, *Appl. Catal., A*, 2007, **333**, 177–191.

42 D. Kulkarni and I. E. Wachs, *Appl. Catal., A*, 2002, **237**, 121–137.

43 F. B. Noronha, A. Frydman, D. A. G. Aranda, C. Perez, R. R. Soares, B. Morawek, D. Castner, C. T. Campbell, R. Frety and M. Schmal, *Catal. Today*, 1996, **28**, 147–157.

44 L. Guczi, G. Boskovic and E. Kiss, *Catal. Rev.*, 2010, **52**, 133–203.

45 J. A. Rodriguez, *Surf. Sci. Rep.*, 1966, **24**, 223–287.

46 Z. Wang, F. Yang, S. Axnanda, C. Liu and D. W. Goodman, *Appl. Catal., A*, 2011, **391**, 342–349.

47 L. Bugyi, A. Berkó, L. Óvári, A. M. Kiss and J. Kiss, *Surf. Sci.*, 2008, **602**, 1650–1658.

48 J. B. Park, S. F. Conner and D. A. Chen, *J. Phys. Chem. C*, 2008, **112**, 5490–5497.

49 L. Óvári, L. Bugyi, Z. Majzik, A. Berkó and J. Kiss, *J. Phys. Chem. C*, 2008, **112**, 18011–18016.

50 L. Bugyi, L. Óvári and J. Kiss, *Surf. Sci.*, 2009, **603**, 2958–2963.

51 H. L. Abbott, A. Aumer, Y. Lei, C. Asokan, R. J. Meyer, M. Sterrer, S. Shaiklutdinov and H.-J. Freund, *J. Phys. Chem. C*, 2010, **114**, 17099–17104.

52 J. Kiss, L. Óvári, A. Oszkó, G. Pótári, M. Tóth, K. Baán and A. Erdőhelyi, *Catal. Today*, 2012, **181**, 163–170.

53 F. Gao, Y. Wang and D. W. Goodman, *J. Phys. Chem. C*, 2010, **114**, 4036–4043.

54 L. Óvári, A. Berkó, N. Balázs, Z. Majzik and J. Kiss, *Langmuir*, 2010, **26**, 2167–2175.

55 S. A. Tenny, J. S. Ratliff, C. C. Roberts, W. He, S. C. Ammal, A. Heyden and D. A. Chen, *J. Phys. Chem. C*, 2010, **114**, 21652–21663.

56 W. F. Egelhoff Jr, *Surf. Sci. Rep.*, 1987, **6**, 253–415.

57 C. Papp and H.-P. Steinrück, *Surf. Sci. Rep.*, 2013, **68**, 446–487.

58 G. Vári, L. Óvári, C. Papp, H.-P. Steinrück, J. Kiss and Z. Kónya, *Phys. Chem. Chem. Phys.*, 2015, **17**, 5124–5132.

59 H. H. Brongersma, M. Draxler, M. de Ridder and P. Bauer, *Surf. Sci. Rep.*, 2007, **62**, 63–109.

60 A. Trovarelli, *Catal. Rev.*, 1996, **38**, 349–520.

61 H. C. Yao and Y. C. Yu Yao, *J. Catal.*, 1984, **86**, 254–265.

62 F. Sadi, D. Duprez, F. Gérard and A. Miloudi, *J. Catal.*, 2003, **213**, 226–234.

63 S. W. Yu, H. H. Huang, C. W. Tang and C. B. Wang, *Int. J. Hydrogen Energy*, 2014, **39**, 20700–20711.

64 F. Esch, S. Fabris, L. Zhou, T. Montini, C. Africh, P. Fornasiero, G. Comelli and R. Rosei, *Science*, 2005, **309**, 752–755.

65 P. Y. Sheng, W. W. Chiu, A. Yee, S. J. Morrison and H. Idriss, *Catal. Today*, 2007, **129**, 313–321.

66 A. M. da Silva, K. R. de Souza, G. Jacobs, U. M. Graham, B. H. Davis, L. V. Mattos and F. V. Noronha, *Appl. Catal., B*, 2011, **102**, 94–109.

67 F. Solymosi and M. Pásztor, *J. Phys. Chem.*, 1985, **89**, 4789–4793.

68 J. T. Yates Jr, T. M. Duncan, S. D. Worley and R. W. Vaughan, *J. Chem. Phys.*, 1979, **70**, 1219–1224.

69 D. A. Bulushev and G. F. Froment, *J. Mol. Catal. A: Chem.*, 1999, **139**, 63–72.

70 R. Dictor and S. Roberts, *J. Phys. Chem.*, 1989, **93**, 2526–2532.

71 D. Li, S. Sakai, Y. Nakagawa and K. Tomishige, *Phys. Chem. Chem. Phys.*, 2012, **14**, 9204–9213.

72 H. Tanaka, R. Kaino, K. Okumura, T. Kizuka, Y. Nakagawa and K. Tomishige, *Appl. Catal., A*, 2010, **378**, 175–186.

This journal is © the Owner Societies 2015

Phys. Chem. Chem. Phys., 2015, **17**, 27154–27166 | **27165**

73 M. J. J. Jak, C. Konstapel, A. van Kreuningen, J. Verhoven and J. W. M. Frenken, *Surf. Sci.*, 2000, **475**, 295–310.

74 A. Berkó, G. Ménesi and F. Solymosi, *Surf. Sci.*, 1997, **372**, 202–210.

75 L. Óvári and J. Kiss, *Appl. Surf. Sci.*, 2006, **252**, 8624–8629.

76 A. Caballero, J. P. Holgado, V. M. Gonzales-delaCruz, S. E. Habas, T. Herranz and H. Salmeron, *Chem. Commun.*, 2010, **46**, 1097–1099.

77 F. Solymosi, *Catal. Rev.*, 1968, **1**, 233–255.

78 M. A. Vannice and R. L. Garten, *J. Catal.*, 1979, **56**, 236–248.

79 F. Solymosi, A. Erdőhelyi and T. Bánsági, *J. Catal.*, 1981, **68**, 371–382.

80 G. Pótári, D. Madarász, L. Nagy, B. László, A. Sápi, A. Oszkó, Á. Kukovecz, A. Erdőhelyi, Z. Kónya and J. Kiss, *Langmuir*, 2013, **29**, 3061–3072.

81 A. Sasahara, C. L. Pang and H. Onishi, *J. Phys. Chem. B*, 2006, **110**, 13453–13457.

82 A. Sasahara, C. L. Pang and H. Onishi, *J. Phys. Chem. B*, 2006, **110**, 17584–17588.

83 G. S. Zafiris and R. J. Gorte, *J. Catal.*, 1993, **139**, 561–567.

84 J. Stubenrauch and J. M. Vohs, *J. Catal.*, 1996, **159**, 50–57.

85 J. Zhou, P. Baddorf, D. R. Mullins and S. H. Overbury, *J. Phys. Chem.*, 2008, **112**, 9336–9345.

86 T. Miyazawa, K. Okumura, K. Kumimori and K. Tomishigi, *J. Phys. Chem. C*, 2008, **112**, 2574–2583.

87 G. Praline, B. E. Koel, R. L. Hance, H. I. Lee and J. M. White, *J. Electron Spectrosc. Relat. Phenom.*, 1980, **21**, 17–30.

88 A. Pfau and K. D. Schierbaum, *Surf. Sci.*, 1994, **321**, 71–80.

89 C. J. Nelin, P. S. Bagus, E. S. Ilton, S. A. Chambers, H. Kuhlenbeck and H.-J. Freund, *J. Quantum Chem.*, 2010, **110**, 2752–2764.

90 M. Schmid, A. Kaftan, H.-P. Steinrück and J. M. Gottfried, *Surf. Sci.*, 2012, **606**, 945–949.

91 C. D. Frost, C. A. McDowell and I. S. Woolsey, *Chem. Phys. Lett.*, 1972, **17**, 320–323.

92 H. Niehus and R. Spitzl, *Surf. Interface Anal.*, 1991, **17**, 287–307.

93 E. Napetschnig, M. Schmid and P. Varga, *Surf. Sci.*, 2004, **556**, 1–10.

27166 | *Phys. Chem. Chem. Phys.*, 2015, **17**, 27154–27166

This journal is © the Owner Societies 2015